ORIGINAL PAPER

Preload effect on nonlinear dynamic behavior of a rigid rotor supported by noncircular gas-lubricated journal bearing systems

Reza Rashidi · Ardeshir Karami mohammadi · Firooz Bakhtiari nejad

Abstract This paper presents the effect of preload, as one of the design parameters, on nonlinear dynamic behavior of a rigid rotor supported by gas-lubricated noncircular journal bearings. A finite element method has been employed to solve the Reynolds equation in static and dynamical states and the dynamical equations are solved using the Runge–Kutta method. To analyze the behavior of the rotor center in horizontal and vertical directions under different operating conditions, dynamic trajectory, power spectra, Poincare maps, and bifurcation diagrams are used. Results of this study reveal how the complex dynamic behavior of two types of noncircular bearing systems comprising periodic, KT-periodic, and quasi-periodic responses of the rotor center varies with changes in preload value.

Keywords Gas-lubricated · Noncircular bearing · Preload · Poincare map · Bifurcation

R. Rashidi · A. Karami mohammadi (✉)
Department of Mechanical Engineering, Shahrood
University of Technology, Shahrood, Iran
e-mail: akaramim@yahoo.com

R. Rashidi
e-mail: rrashidi@shahroodut.ac.ir

F. Bakhtiari nejad
Department of Mechanical Engineering, Amirkabir
University of Technology, Tehran, Iran
e-mail: baktiari@aut.ac.ir

Nomenclature

$\bar{C}$	Conventional radial clearance (m)
$\bar{C}_m$	Minor clearance when rotor and bearing geometric centers are coincident (m)
$\bar{D}$	Rotor diameter (m)
$\bar{F}_{X_0}, \bar{F}_{Y_0}$	Components of the fluid film force on the rotor in the steady state (N)
$\bar{F}_X, \bar{F}_Y$	Components of the fluid film force on the rotor in the dynamical state (N)
$\bar{W}_0$	Static load (N)
$\bar{h}$	Film thickness (m)
$\bar{L}$	Bearing length (m)
$\bar{m}_r$	Rotor mass (Kg)
N_i	Shape function
n_e	Number of nodes in an element
n_f	Number of nodes in fluid domain
$\bar{P}^*$	Absolute gas pressure (N/m^2)
$\bar{P}$	Partial gas pressure (N/m^2)
$\bar{P}_a$	Ambient pressure (N/m^2)
$\bar{R}$	Rotor radius (m)
$\bar{t}$	Time (s)
$\bar{U}$	Peripheral speed of the rotor in dynamical state (m/s)
$\bar{X}, \bar{Y}$	Cartesian axes with origin at the bearing geometric center (m)
$\bar{X}_{j0}, \bar{Y}_{j0}$	Coordinates of the rotor center in steady state (m)
$\bar{X}_j, \bar{Y}_j$	Coordinates of the rotor center in dynamical state (m)

$\bar{x}, \bar{y}$ Perturbation coordinates of the rotor center measured from its static equilibrium position (m)

V_x, V_y Dimensionless velocity of the rotor center in horizontal and vertical directions

A_x, A_y Dimensionless acceleration of the rotor center in horizontal and vertical directions

δ Preload in the bearing ($\bar{C}_m/\bar{C}$)

λ Bearing aspect ratio ($\bar{L}/\bar{D}$)

Λ Bearing number

$\bar{\mu}$ Ambient dynamic viscosity of the lubricant (N s/m^2)

θ Angular coordinate measured from X-axis

θ_0^k Angle of lobe line of centers

θ_1^k, θ_2^k Angles at the leading and trailing edge of the lobe

$\bar{\omega}$ Rotational speed of the rotor (rad/s)

$\bar{\rho}$ Mass eccentricity of the rotor (m)

τ Dimensionless time

$\bar{\xi}$ Coordinate along bearing axis measured from mid span (m)

superscripts

e Element numbers

k Lobe designation

subscript

0 Static equilibrium position of the rotor bearing at $\tau = 0$

1 Introduction

During the past few decades, gas-lubricated bearings have received great attention of practical and analytical tribologists. The rapid growth of gas bearing technology is mainly due to its wide range of engineering application such as precision machine tools, high speed aircraft, nuclear reactors, textile spindles, dental drills, etc. Gas-lubricated journal bearings have the advantage of negligible friction, cleanliness and easy availability of air as the lubricant; however, poor dynamic stability due to low viscosity is a major problem. Therefore, investigation of dynamical behavior is necessary to avoid settling of the system in a region that its control is severe.

In 1961, Castelli and Elrod [1] made a significant contribution toward a better understanding of the complex fluid dynamic phenomenon in gas lubrication.

These authors presented their assessment of the validity of the assumptions made in the analysis of earlier investigators. They neglected the pressure time derivative term in the Reynolds equation and obtained the rotor center orbits for a specified set of operating and initial conditions by numerical integration of the equations of motion of the rotor.

Ausman [2] solved the linearized Reynolds equation of self-acting bearings to investigate the stability of the static equilibrium position of the rotor. In 1978, Holmes et al. [3] discussed aperiodic behavior in short journal bearings. They noted that a moderate level of unbalance and a high eccentricity ratio led to an aperiodic response of the shaft at speeds above a critical threshold value. Chandra et al. [4] studied static and dynamic characteristics of four gas lubricated noncircular journal bearing configurations. In their work, the linearized Reynolds equation was solved by the finite element method and a comparative stability analysis was done. In 1994, Zhao et al. [5] investigated nonlinear dynamic behavior of an eccentric squeeze film damper-mounted rigid rotor system. The authors showed that for large values of unbalance and static misalignment, the subharmonic and quasi-periodic motions generated at speeds of more than twice the system critical speed were bifurcated from the unbalance harmonic solution.

Nonlinear dynamic behavior such as subharmonic, quasi-periodic, and chaotic motions for suitable values of system parameters in a rigid rotor supported by short bearings were reported by Adiletta et al. through the theoretical and experimental investigations [6–8]. Czolczynski and Kapitaniak [9] described a method which allows controlling the Hopf bifurcation of a rotor system supported by two gas bearings. They showed the damage caused by the growing amplitude of self-excited vibrations, can be avoided by a proper selection of stiffness and damping coefficients of the air ring.

Nonlinear dynamic and bifurcation analysis of a rigid rotor [10] and flexible rotor [11] supported by self-acting gas journal bearing were studied by Wang et al. In both works, by considering rotor mass and rotational speed as the parameters of system, periodic and subharmonic motions of the rotor center were reported. In 2005, Wang Jiun-Shen and Wang Cheng-Chi [12] presented bifurcation of a rigid rotor by relative short aerodynamic journal bearings. They discussed how the existence of a complex dynamic behavior comprises periodic and subharmonic responses

of the rotor center. Also, Wang [13] provided a further understanding of a rigid rotor supported by a relatively short externally pressurized porous gas journal bearing and showed the dynamic behavior of the system with respect to rotor mass and bearing number.

In 2007, Wang et al. studied the behavior of a rigid rotor [14] and a flexible rotor [15] supported by a herringbone-grooved gas journal bearing system. Their analysis revealed a complex dynamic behavior comprising periodic and quasi-periodic responses of the system. Rahmatabadi and Rashidi investigated static and dynamic characteristics of noncircular gas-lubricated journal bearings by considering the effect of mount angle [16] and preload [17]. They showed noncircular bearings have better dynamic characteristics than circular bearings. Also, by using suitable value of mount angle stability margin can be increased.

Although previous works provide insight into the behavior of the system, but the bifurcation and nonlinear dynamic behavior of the gas film in a gas-lubricated noncircular journal bearing has been not examined. Therefore, this paper presents the effect of preload on nonlinear dynamic behavior of a rigid rotor supported by three-lobe and four-lobe bearings (Fig. 1).

The amount of preload of a noncircular bearing determines its noncircularity or ellipticity relative to a plane journal bearing. For zero preload, the rotor touches the lobes at their line of centers while with unit preload a lobed bearing reduces into an axial groove plane journal bearing.

Due to the nonlinearity of the gas film pressure, it is very difficult to solve the Reynolds equation analytically. Therefore, finite element methods have been employed to obtain the solution and then the Runge–Kutta method has been used to solve this equation and equations of motion simultaneously to obtain position, velocity, and acceleration of rotor center.

2 Mathematical analysis

2.1 Governing equations

The geometric details of two types of noncircular bearing configurations are shown in Fig. 1.

Analysis of gas-lubricated noncircular bearing involves solution of the governing equations separately for an individual lobe of the bearing, treating each lobe as an independent partial bearing. To generalize the analysis for all noncircular geometries, the film geometry of each lobe is described with reference to bearing fixed Cartesian axes (Fig. 1). Thus, the film thickness in the clearance space of the kth lobe, with the rotor in a dynamical state is expressed by

$$
\bar{h} = \bar{C} - (\bar{X}_j)\cos\theta - (\bar{Y}_j)\sin\theta + (\bar{C} - \bar{C}_m)\cos(\theta - \theta_0^k),
\tag{1}
$$

where $(\bar{X}_j, \bar{Y}_j)$ is the rotor center coordinate in the dynamical state and θ_0^k is angle of lobe line of centers. $\bar{C}$ and $\bar{C}_m$ are conventional radial clearance and minor clearance, when journal and bearing geometric centers are coincident. The pressure governing equation of isothermal flow field in a bearing lobe is modeled by the Reynolds equation:

$$
\frac{\partial}{\partial \bar{X}}\left\{\bar{h}^3 \bar{P}^* \frac{\partial \bar{P}^*}{\partial \bar{X}}\right\} + \frac{\partial}{\partial \bar{Y}}\left\{\bar{h}^3 \bar{P}^* \frac{\partial \bar{P}^*}{\partial \bar{Y}}\right\}
$$
$$
= 6\bar{\mu}\left[\bar{U}\frac{\partial}{\partial \bar{X}} + 2\frac{\partial}{\partial \bar{t}}\right](\bar{P}^* \bar{h})
\tag{2}
$$

in which $\bar{P}^*$ is the absolute gas pressure, $\bar{\mu}$ is the gas viscosity, $\bar{U}$ is the peripheral speed of the rotor and $\bar{t}$ is the time.

It will be more convenient to express $\bar{P}^*$ as

$$
\bar{P}^* = \bar{P}_a + \bar{P},
\tag{3}
$$

where $\bar{P}_a$ and $\bar{P}$ are the ambient and partial pressure, respectively.

In order to nondimensionalize (1) and (2), let

$$
\bar{C}_m = \bar{C}\delta, \qquad (\bar{X}_j, \bar{Y}_j) = \bar{C}_m(X_j, Y_j), \qquad \bar{X} = \bar{R}\theta,
$$
$$
\bar{Y} = \bar{R}\xi, \qquad \bar{h} = \bar{C}_m h, \qquad \bar{P} = \bar{P}_a P,
$$
$$
\bar{U} = \bar{U}_0 U = \bar{R}\bar{\omega}_0 U, \qquad \bar{t} = \frac{\tau}{\bar{\omega}_0}
$$

which $\bar{\omega}_0$ is the rotational speed in the steady state and $\bar{R}$ is the rotor radius. Substituting these variables in (1), the nondimensional film thickness can be obtained as

$$
h = \frac{1}{\delta} - (X_j)\cos\theta - (Y_j)\sin\theta + \left(\frac{1}{\delta} - 1\right)\cos(\theta - \theta_0^k)
\tag{4}
$$

Fig. 1 (**a**) Model of a rigid
rotor supported by two
gas-lubricated noncircular
journal bearings, (**b**) cross
section of a three-lobe
bearing, and (**c**) cross
section of a four-lobe
bearing
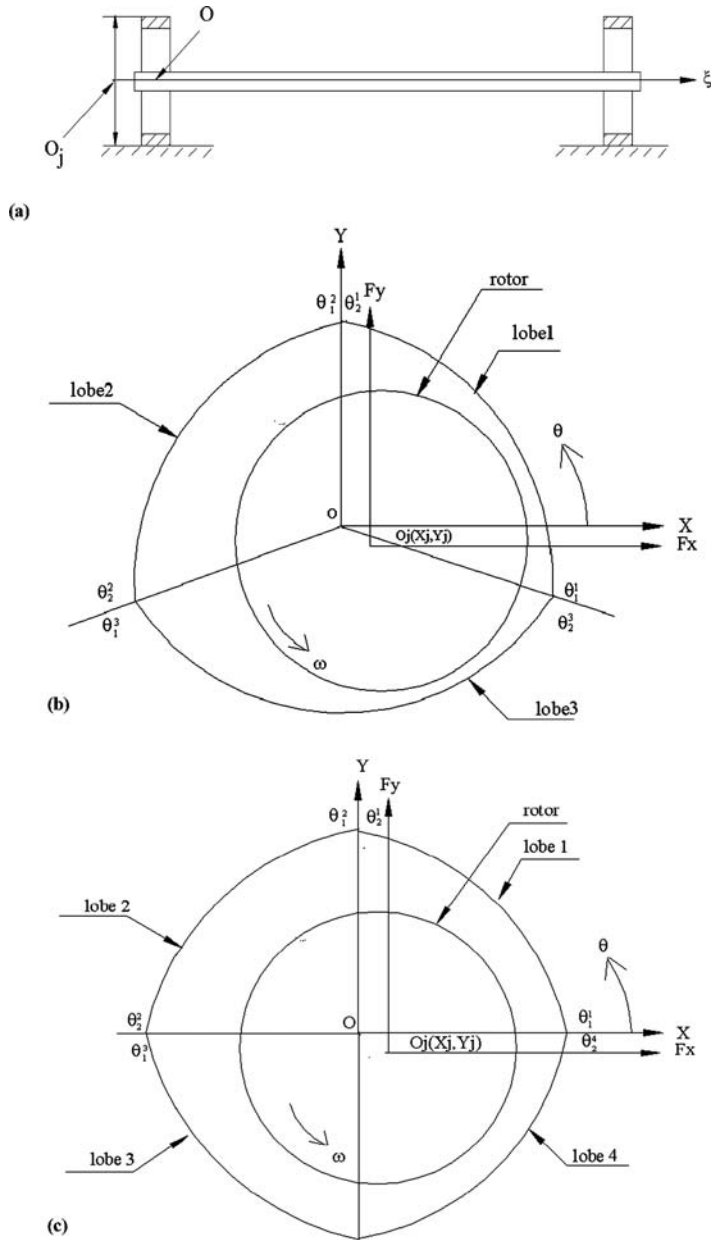
and by substituting (3) in (2) and simplifying, the
Reynolds equation in nondimensional form can be expressed by

$$\frac{\partial}{\partial\theta}\left\{h^3(P+1)\frac{\partial P}{\partial\theta}\right\} + \frac{\partial}{\partial\xi}\left\{h^3(P+1)\frac{\partial P}{\partial\xi}\right\}$$

$$= \Lambda\left[U\frac{\partial}{\partial\theta} + 2\frac{\partial}{\partial\tau}\right]\{(P+1)h\}, \tag{5}$$

where θ and ξ are the coordinates in the circumferential and axial directions, respectively, and

$$\Lambda = \frac{6\bar{\mu}\bar{\omega}_0\bar{R}^2}{\bar{P}_a\bar{C}_m^2}$$

is the dimensionless parameter called the compressibility number or bearing number.

The Reynolds equation is a nonlinear partial differential equation, therefore, can be solved using finite

element method. For this purpose, let the function variable

$$\Psi = \Psi(\tau) = Ph$$

be introduced into (5) which then becomes

$$\frac{\partial}{\partial \theta}\left\{ h(\Psi + h)\frac{\partial \Psi}{\partial \theta} - (\Psi + h)\Psi\frac{\partial h}{\partial \theta}\right\}$$

$$+ \frac{\partial}{\partial \xi}\left\{ h(\Psi + h)\frac{\partial \Psi}{\partial \xi}\right\}$$

$$= \Lambda\left(U\frac{\partial}{\partial \theta} + 2\frac{\partial}{\partial \tau}\right)(\Psi + h). \tag{6}$$

For the finite element formulation, the Galerkin's weighted residual of (6) for an element of the discretized space domain of Ψ field is written as

$$\iint_{A^e}\left[\frac{\partial \Psi^e}{\partial t} - \frac{1}{2\Lambda}\frac{\partial}{\partial \theta}\right.$$

$$\times\left\{ h\big(\Psi^e + h\big)\frac{\partial \Psi^e}{\partial \theta} - \big(\Psi^e + h\big)\Psi^e\frac{\partial h}{\partial \theta}\right\}$$

$$- \frac{1}{2\Lambda}\frac{\partial}{\partial \xi}\left\{ h\big(\Psi^e + h\big)\frac{\partial \Psi^e}{\partial \xi}\right\}$$

$$\left. + \frac{1}{2}U\frac{\partial}{\partial \theta}\big(\Psi^e + h\big) + \frac{\partial h}{\partial \tau}\right] N_i^e\, d\theta\, d\xi = 0, \tag{7}$$

where N_i^e is an approximation function and A^e is the area of the element. By considering the discretized domain of Ψ variable and let, in an element "e," the Ψ function be approximated by

$$\Psi^e = \sum_{j=1}^{n_e} N_j^e \Psi_j(\tau) \tag{8}$$

in which "e" refers to an element, n_e is the number of nodes in the element, N_j^e's are the shape functions and Ψ_j's are the nodal values of Ψ at time τ. Using (8) in (7) and with some integral simplification, the finite element equations for an element of the discretized flow filed domain can be obtained as

$$[F]^e\{\dot{\Psi}\}^e = \{V\}^e + \{Q\}^e \tag{9}$$

in which the components of the element matrices are

$$F_{ij}^e = \iint_{A^e} N_i^e N_j^e\, d\theta\, d\xi, \tag{10a}$$

$$V_i^e = -\frac{1}{2\Lambda}\iint_{A^e}\big(\Psi^e + h\big)$$

$$\times \left\{ h\left(\frac{\partial \Psi^e}{\partial \theta}\frac{\partial N_i^e}{\partial \theta} + \frac{\partial \Psi^e}{\partial \xi}\frac{\partial N_i^e}{\partial \xi}\right)\right.$$

$$\left. - \left(\Psi^e\frac{\partial h}{\partial \theta} + \Lambda U\right)\frac{\partial N_i^e}{\partial \theta}\right\} d\theta\, d\xi$$

$$- \iint_{A^e}\frac{\partial h}{\partial \tau}N_i^e\, d\theta\, d\xi, \tag{10b}$$

$$Q_i^e = \int_{S^e}\big(\Psi^e + h\big)\left\{ h\frac{\partial \Psi^e}{\partial \theta} - \Psi^e\frac{\partial h}{\partial \theta} - \Lambda U\right\}$$

$$\times N_i^e\, d\xi + \int_{S^e}\big(\Psi^e + h\big)h\frac{\partial \Psi^e}{\partial \xi}N_i^e\, d\theta, \tag{10c}$$

where S^e is the boundary of the element.

The assembly of (8) for all elements of Ψ domain yields the global equations.

$$[F]_{n_f \times n_f}\{\dot{\Psi}\}_{n_f \times 1} = \{V\}_{n_f \times 1} + \{Q\}_{n_f \times 1}, \tag{11}$$

where n_f is the total number of nodes.

The boundary conditions of the variables for the solution of (11) are

$$\Psi\big(\theta_1^k, \zeta, \tau\big) = \Psi\big(\theta_2^k, \zeta, \tau\big) = 0,$$

$$\dot{\Psi}\big(\theta_1^k, \zeta, \tau\big) = \dot{\Psi}\big(\theta_2^k, \zeta, \tau\big) = 0,$$

$$\Psi(\theta, \pm\lambda, \tau) = 0,$$

$$\dot{\Psi}(\theta, \pm\lambda, \tau) = 0. \tag{12}$$

At any instant when the kinematic state of the rotor center is known, (11) comprises two variables, Ψ_i and Q_i to be determined. However, at the internal nodes of the discretized space domain, the flux Q_i is zero and Ψ_i is unknown. At the nodes on the boundaries $\xi = \pm\lambda$, and edges of the lobes (θ_1^k and θ_2^k), Ψ_i is known while Q_i is not known. Thus, (11) really involves as many unknowns as the number of equations and may be solved by invoking the boundary conditions. The solution of these equations yields

$$\{\dot{\Psi}\}_{n_f \times 1} = \{g\}_{n_f \times 1}, \tag{13}$$

where $g_i = g_i(P, \tau); i = 1, 2, \ldots, n_f.$

2.2 Rotor dynamic equations and computation procedure

In the dynamical state, the equations of motion of the rotor can be written as

$$\bar{m}_r \frac{d^2 \bar{x}}{d\bar{t}^2} = (\bar{F}_X - \bar{F}_{X0}) + \bar{m}_r \bar{\rho} \bar{\omega}^2 \cos \bar{\omega} \bar{t}, \tag{14}$$

$$\bar{m}_r \frac{d^2 \bar{y}}{d\bar{t}^2} = (\bar{F}_Y - \bar{F}_{Y0}) + \bar{m}_r \bar{\rho} \bar{\omega}^2 \sin \bar{\omega} \bar{t}, \tag{15}$$

$\bar{m}_r$ is the mass of rotor, $\bar{\rho}$ is the mass eccentricity of the rotor and $\bar{\omega}$ is the rotational speed. $(\bar{x}, \bar{y})$ is the perturbed position of the rotor center that defined as

$$\bar{x} = \bar{X}_j - \bar{X}_{j0}, \bar{y} = \bar{Y}_j - \bar{Y}_{j0} \tag{16}$$

also, $(\bar{F}_X, \bar{F}_Y)$ and $(\bar{F}_{X0}, \bar{F}_{Y0})$ are the components of fluid film force on the rotor in the dynamical and steady states, respectively.

The components of fluid film force on the rotor are given by

$$\begin{Bmatrix} \bar{F}_X - \bar{F}_{X0} \\ \bar{F}_Y - \bar{F}_{Y0} \end{Bmatrix} = -\bar{P}_a \bar{R}^2 \iint_A (P - P_0) \begin{Bmatrix} \cos \theta \\ \sin \theta \end{Bmatrix} d\theta \, d\xi, \tag{17}$$

where, A is the pressure area on the rotor, $P_0 = P_0(X_{j0}, Y_{j0})$ and $P = P(X_j, Y_j, V_x, V_y, \tau)$ are the film pressure in the steady state and dynamical state, respectively.

The following transformation is introduced

$$x = \bar{x}/\bar{C}_m, \qquad y = \bar{y}/\bar{C}_m$$

and defining nondimensional groups

$$F_X = \frac{\bar{F}_X}{\bar{P}_a \bar{R}^2}, \qquad F_{X0} = \frac{\bar{F}_{X0}}{\bar{P}_a \bar{R}^2}, \qquad F_Y = \frac{\bar{F}_Y}{\bar{P}_a \bar{R}^2},$$

$$F_{Y0} = \frac{\bar{F}_{Y0}}{\bar{P}_a \bar{R}^2}, \qquad m_r = \frac{\bar{m}_r \bar{C}_m \bar{\omega}^2}{\bar{P}_a \bar{R}^2}, \qquad \rho = \frac{\bar{m}_r \bar{\rho} \bar{\omega}^2}{\bar{P}_a \bar{R}^2}$$

substituting these nondimensional groups into (14)–(15) yields

$$A_x = \frac{d^2 x}{d\tau^2} = \frac{F_X - F_{X0}}{m_r} + \frac{\rho}{m_r} \cos \tau, \tag{18}$$

$$A_y = \frac{d^2 y}{d\tau^2} = \frac{F_Y - F_{Y0}}{m_r} + \frac{\rho}{m_r} \sin \tau. \tag{19}$$

By defining the state variable,

$$S_1 = x, \qquad S_2 = y, \qquad S_3 = V_x, \qquad S_4 = V_y \tag{20}$$

Table 1 Comparison of rotor center orbit data calculated by finite difference method (FDM) and finite element method (FEM)

Type	δ	Method	x			y		
			$\tau = 10$	$\tau = 100$	$\tau = 1000$	$\tau = 10$	$\tau = 100$	$\tau = 1000$
Three-lobe	0.4	FEM	–	–	0.049960	0.029917	–	–
			0.035925	0.021680			0.041373	0.012965
		FDM	–	–	0.049605	0.029209	–	–
			0.035884	0.021023			0.041057	0.012494
	0.5	FEM	0.053011	–	–	0.025801	–	–
				0.082651	0.011911		0.037887	0.070015
		FDM	0.052214	–	–	0.026623	–	–
				0.082480	0.011132		0.038472	0.069683
Four-lobe	0.4	FEM	–	–	0.034625	0.015963	–	0.001221
			0.029450	0.007134			0.032084	
		FDM	–	–	0.034124	0.015174	–	0.001588
			0.029190	0.006686			0.031490	
	0.5	FEM	0.035754	–	0.020073	0.064393	–	–
				0.068212			0.058021	0.047436
		FDM	0.033392	–	0.021221	0.063349	–	–
				0.067159			0.058758	0.045936
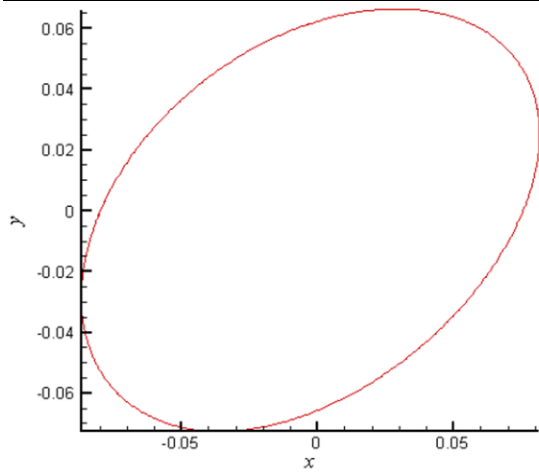
2.1(a)
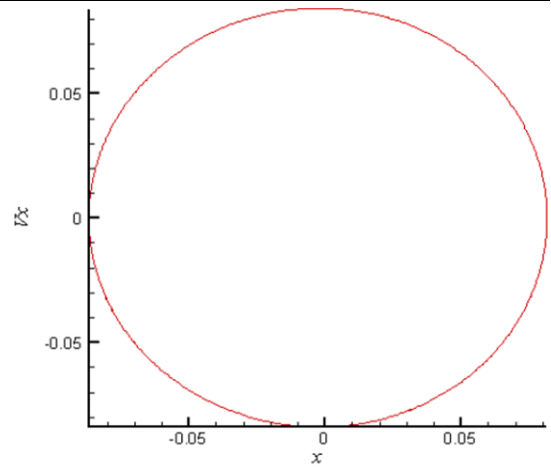
2.1(b)
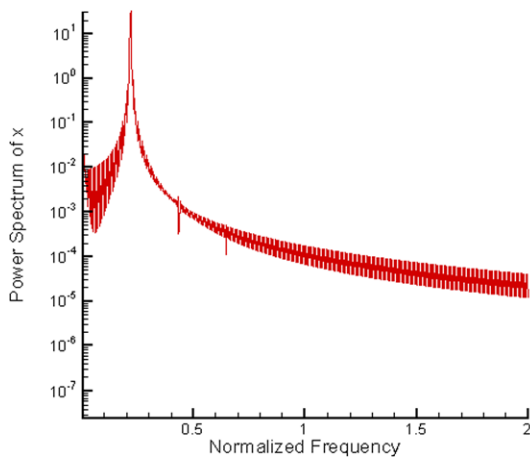
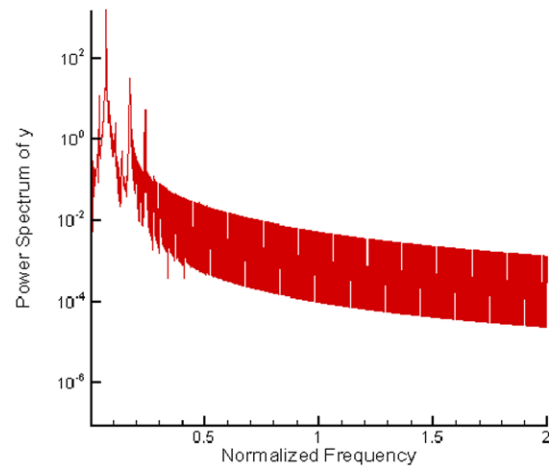**2.1(c)**
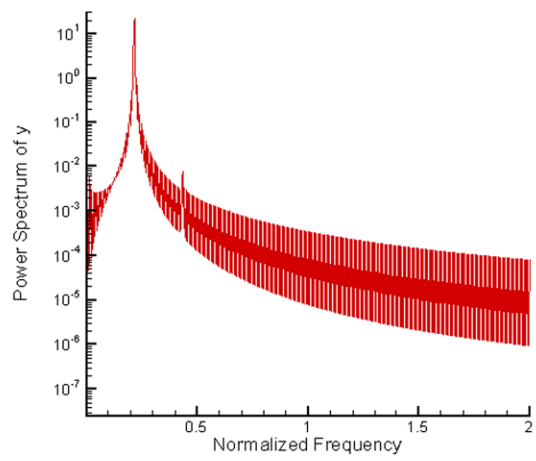
2.1(d)
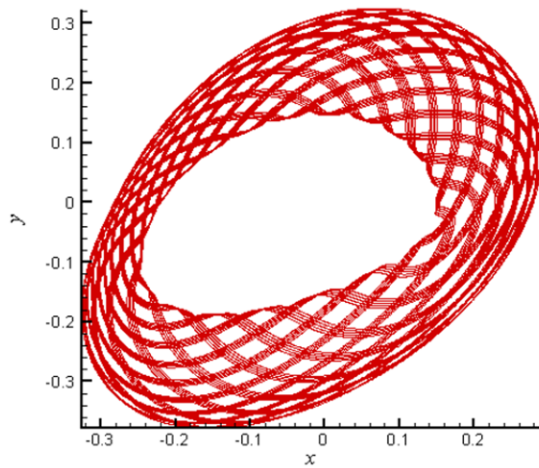
2.2(a)
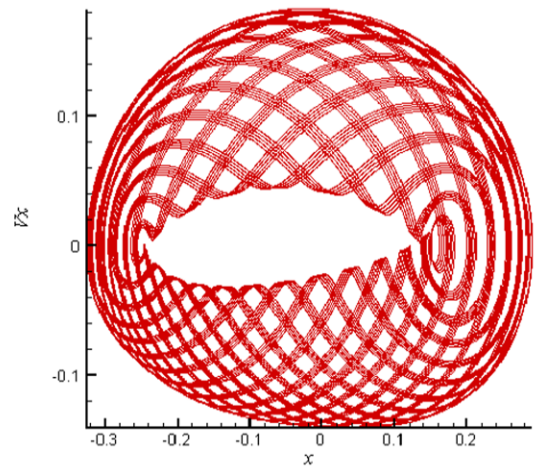
2.2(b)

Fig. 2 Trajectory of the rotor center at $\delta = 0.48$, 0.542, 0.544, 0.55, 0.554, 0.56, 0.576 and 0.584 (**2.1(a)**–**2.8(a)**); phase portraits of rotor cen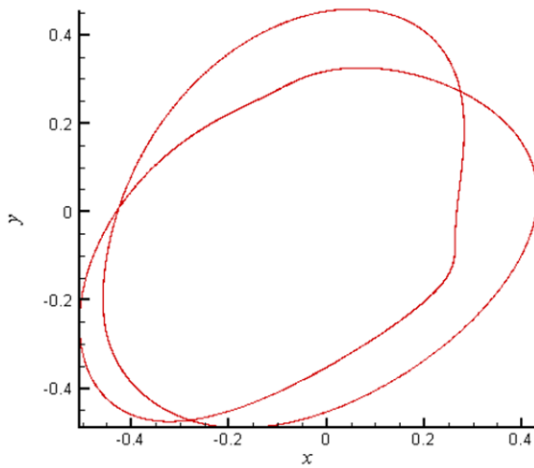ter (**2.1(b)**–**2.8(b)**) and power spectra of rotor displacement in horizontal (**2.1(c)**–**2.8(c)**) and vertical (**2.1(d)**–**2.8(d)**)) directions for three-lobe
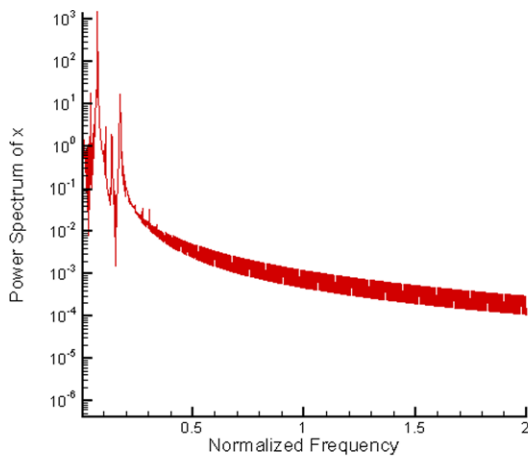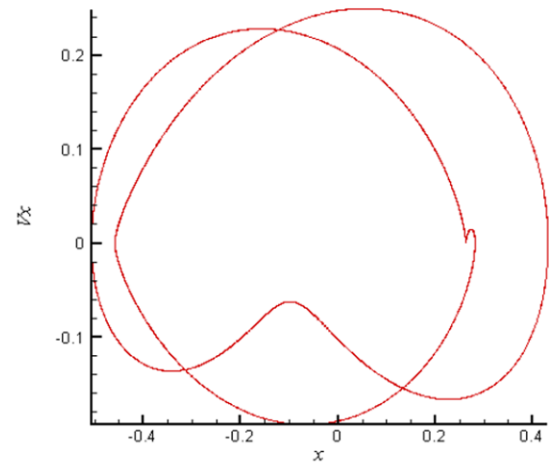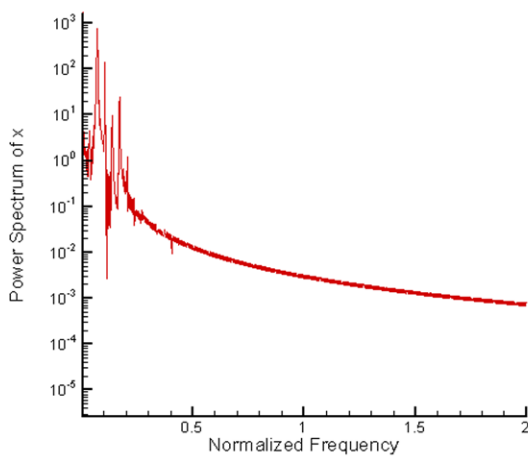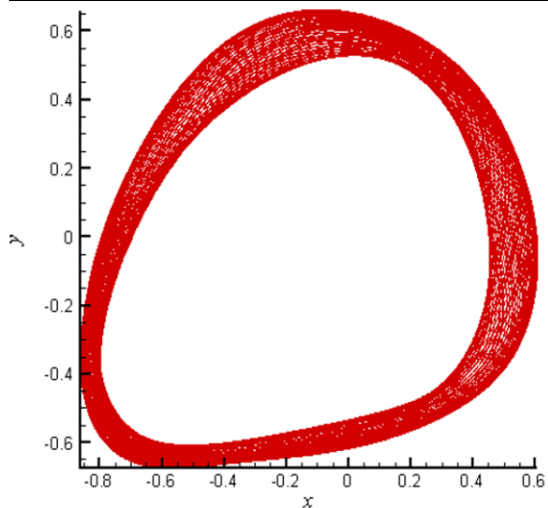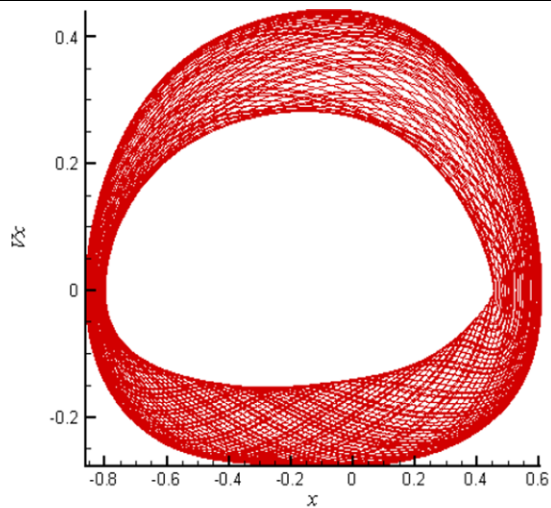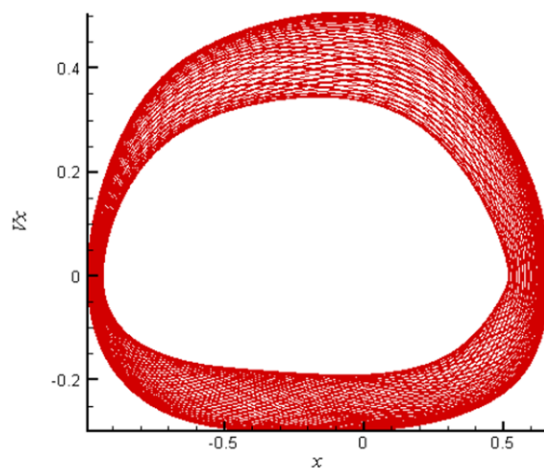
2.2(c)

2.2(d)

2.3(a)

2.3(b)

2.3(c)
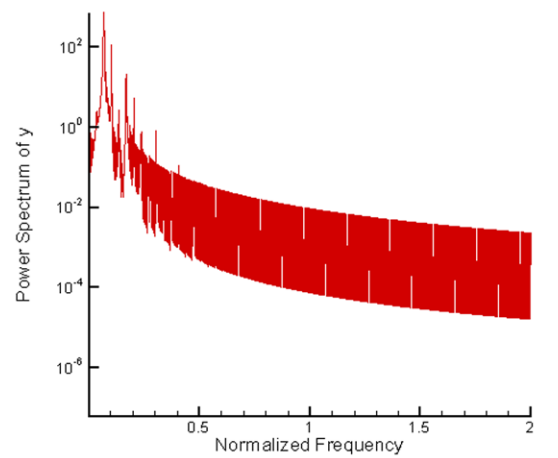
2.3(d)

Fig. 2 (*Continued*)

2.4(a)

2.4(b)
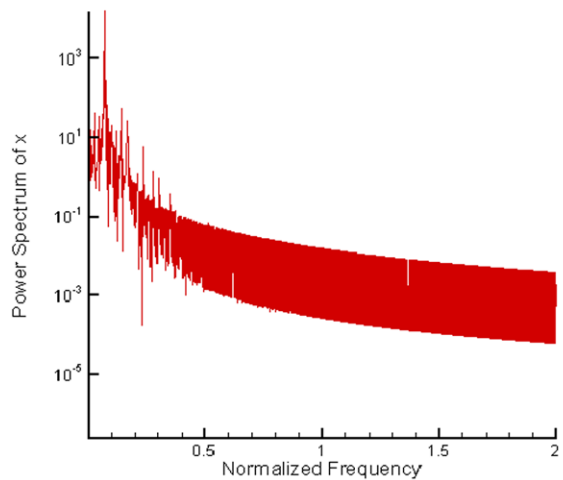
2.4(c)
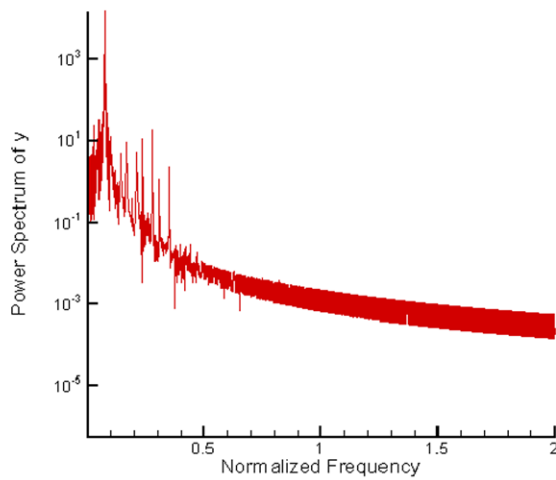
2.4(d)
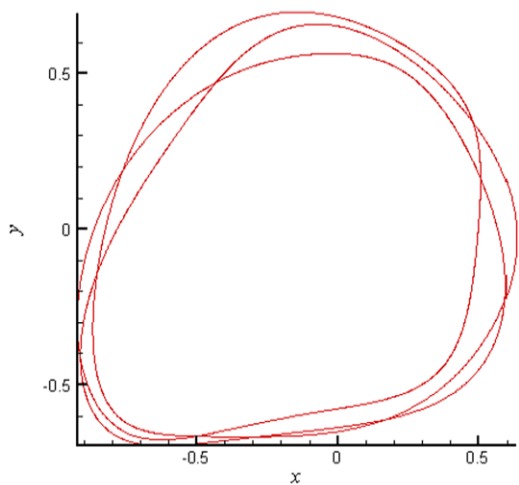
2.5(a)
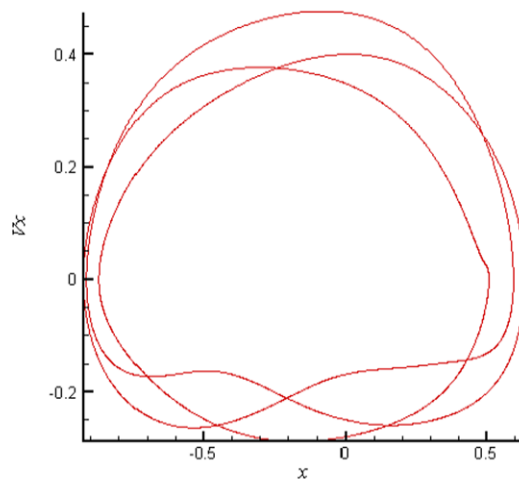
2.5 (b)

Fig. 2 (*Continued*)
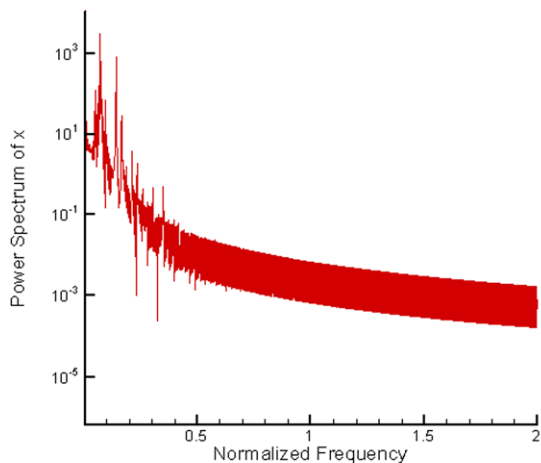
2.5(c)
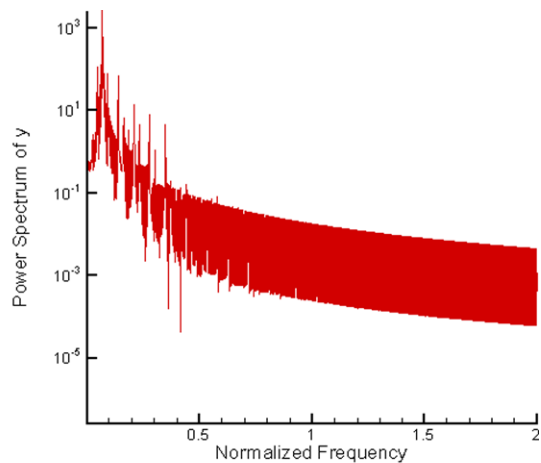
2.5(d)
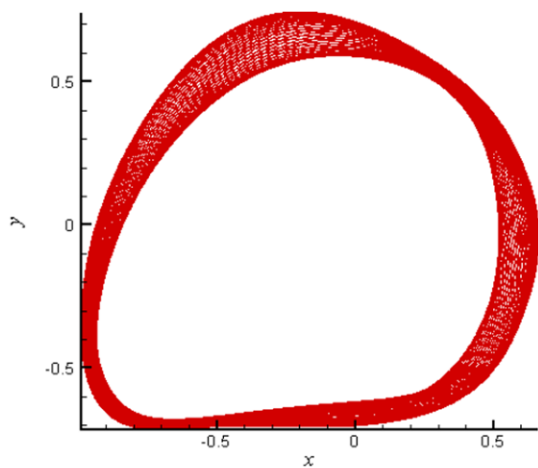
2.6(a)

2.6(b)
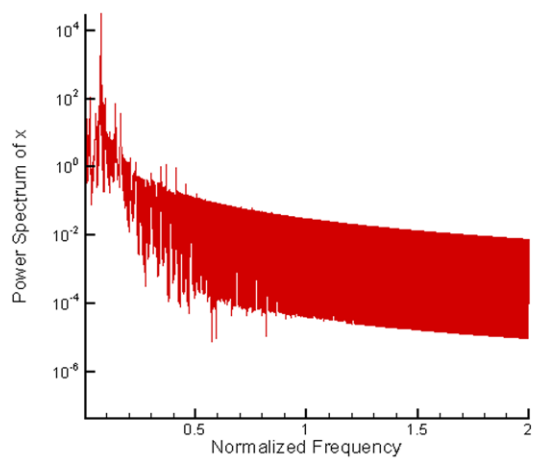
2.6(c)
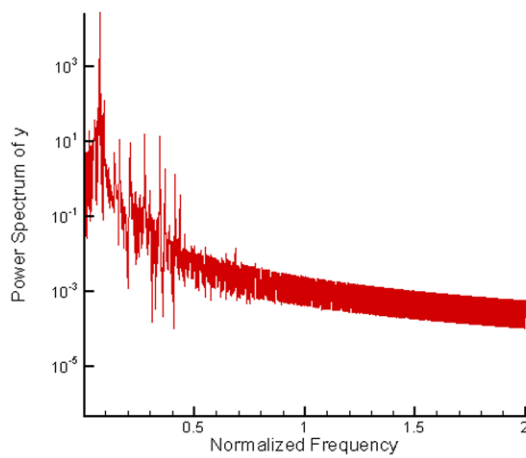
2.6(d)

Fig. 2 (*Continued*)
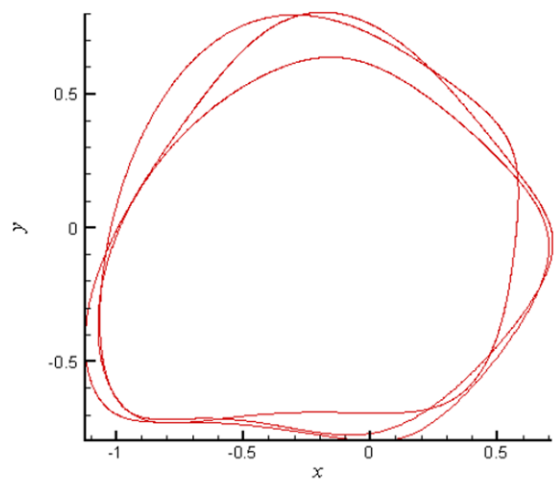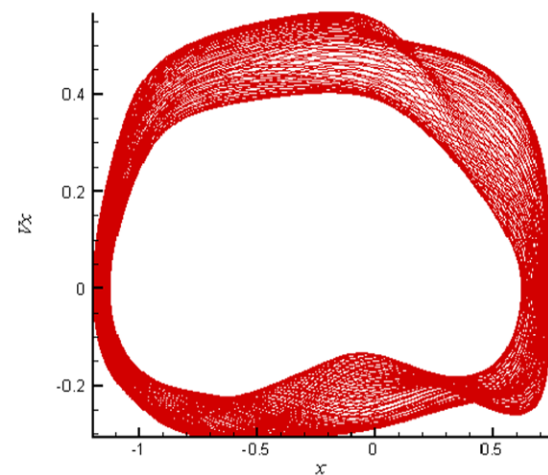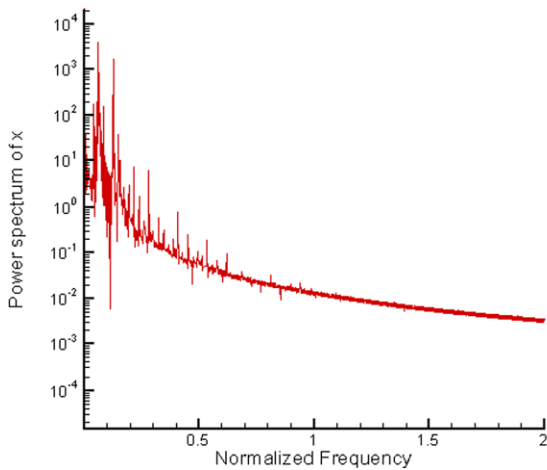
2.7(a)
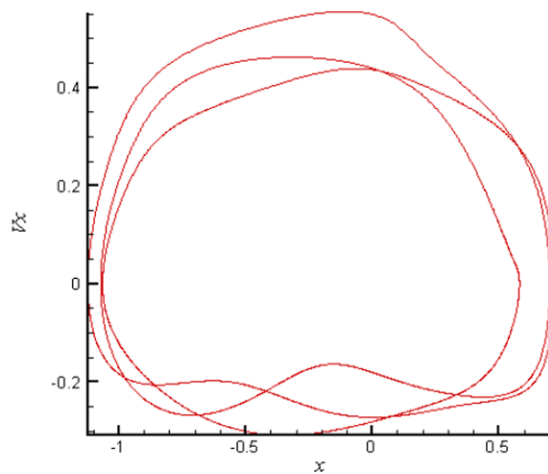
2.7(b)
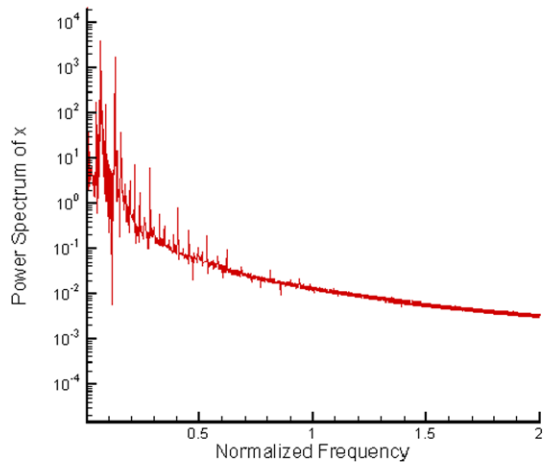
2.7(c)
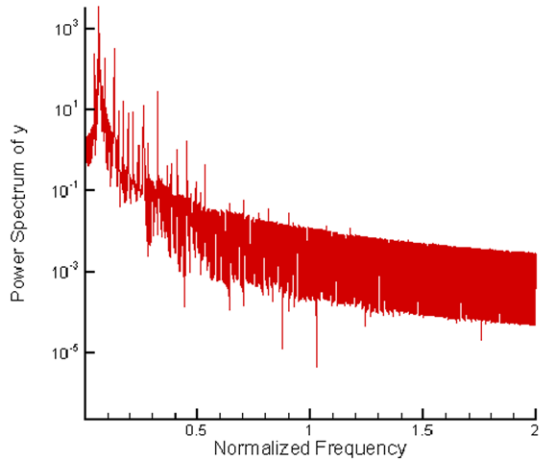
2.7(d)
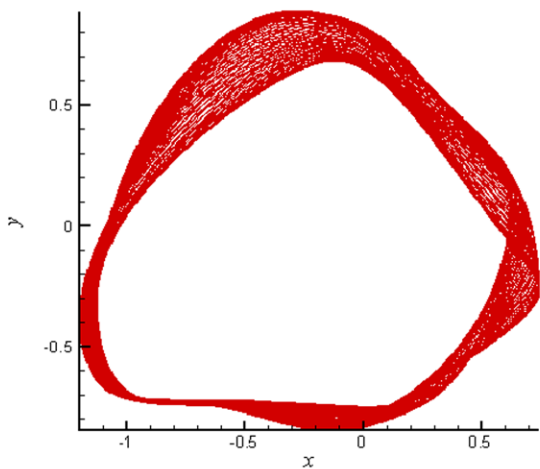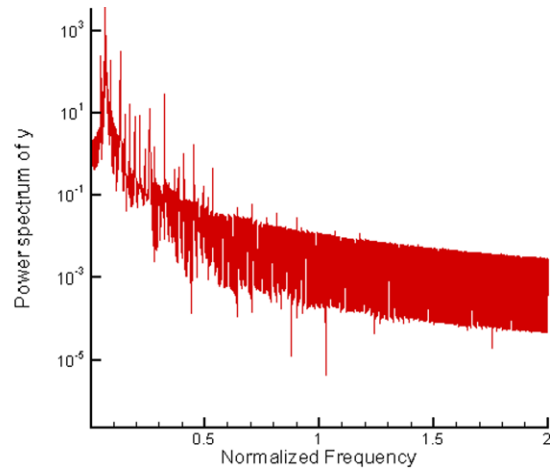

2.8(a)

2.8(b)

Fig. 2 (*Continued*)

2.8(c)

2.8(d)

Fig. 2 (*Continued*)

the equations of motion are transformed to the following state space equations as

$$\frac{dS_1}{d\tau} = S_3, \tag{21}$$

$$\frac{dS_2}{d\tau} = S_4, \tag{22}$$

$$\frac{dS_3}{d\tau} = \frac{F_X - F_{X0}}{m_r} + \frac{\rho}{m_r}\cos\tau, \tag{23}$$

$$\frac{dS_4}{d\tau} = \frac{F_Y - F_{Y0}}{m_r} + \frac{\rho}{m_r}\sin\tau. \tag{24}$$

Equations (13) and (21)–(24) describe a nonlinear dynamic system. The equations are restated for convenience

$$\frac{dS_i}{d\tau} = f_i(P, S_1, S_2 S_3, S_4, \tau), \quad i = 1, 2, 3, 4,$$

$$\frac{d\Psi_i}{d\tau} = g_i(P, S_1, S_2 S_3, S_4, \tau), \quad i = 1, 2, \ldots, n_f. \tag{25}$$

The procedure starts with the journal at the equilibrium position. Therefore, at the beginning, Reynolds equation should be solved in the steady state to obtain Ψ_0 and (X_{j0}, Y_{j0}). Meanwhile, the initial velocity of the rotor is assumed to be zero. The numerical integration of (25) is carried out by the fourth-order Runge–Kutta method. By this method, acceleration, velocity, and displacement of the rotor are estimated at each time step and are utilized to initial conditions for the

next time step. Then the displacement of the rotor center obtained from each step is used to update the film thickness and the new pressure distribution can be obtained to yield the new dynamical force by integrating it.

3 Numerical studies

Due to the high nonlinearity of gas film forces, the system behavior is studied numerically using the finite element method. In this study, the time step for the calculation is $\pi/300$ and the error tolerance is less than 10^{-6}. The time series data of the first 600,000 time steps are excluded from dynamic behavior investigation to ensure that the data used represent steady state conditions. The resulting data include the orbital paths of the rotor center. These data are then used to generate the power spectra, Poincare maps, and bifurcation diagrams.

Fast Fourier transformation is used to obtained power spectra of the rotor center in horizontal and vertical directions.

To generate Poincare map, a Poincare section that is transverse to the flow of a given dynamic system is considered. A point on this section is a return point of the time series at the constant time interval of T, that T is the driven period of the exciting force in nonautonomous systems. The projection of a Poincare section on the x–y plane is related to the Poincare map of the dynamic system. The points obtained in the

Fig. 3 Bifurcation diagrams: (**a**) $x(nT)$ and (**b**) $y(nT)$ versus preload for three-lobe bearing
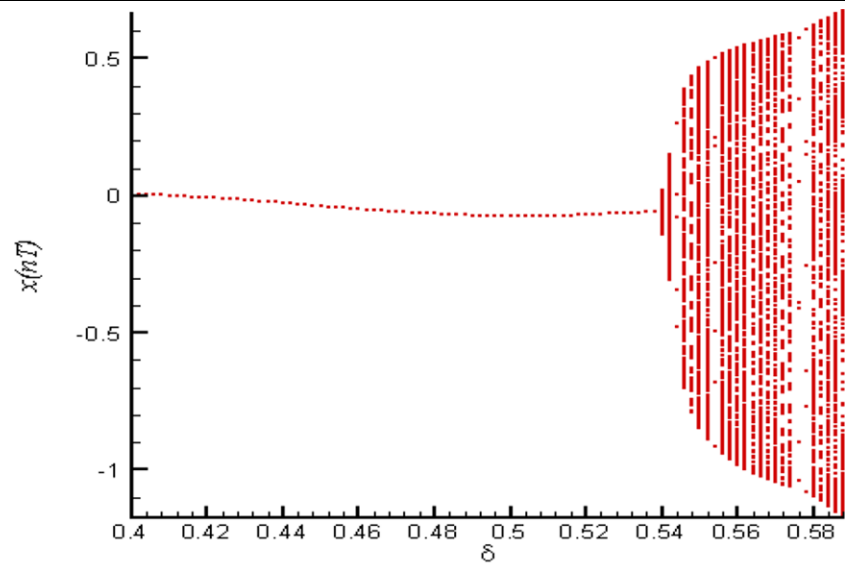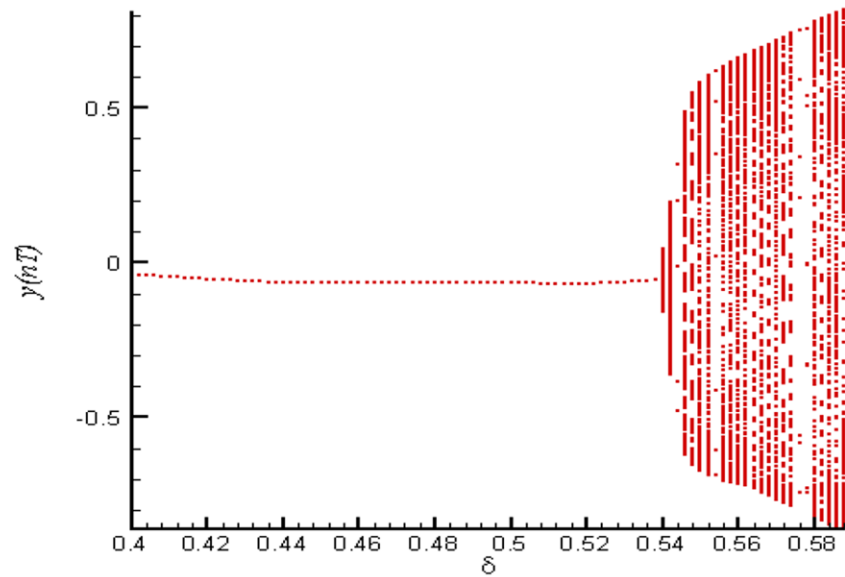
Poincare map are used to draw bifurcation diagrams with varying preload as a parameter of system by a constant step.
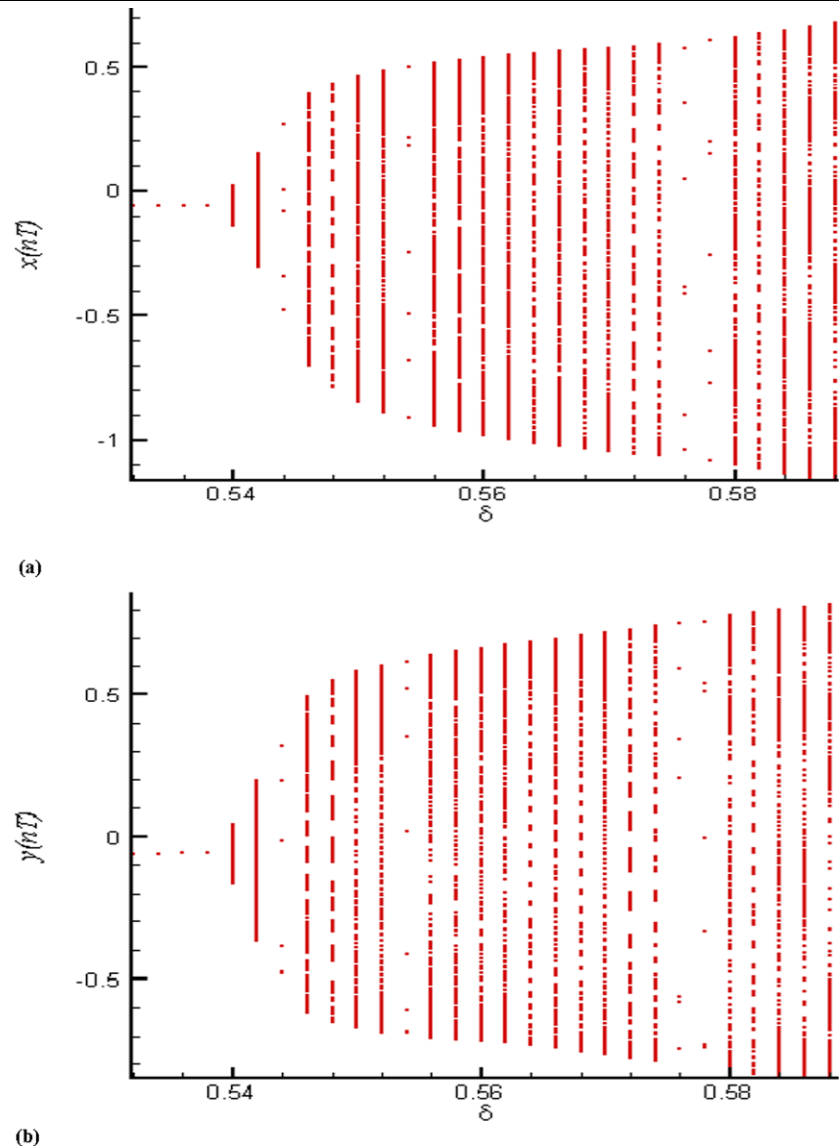
4 Results and discussion

In this section, by considering preload as the bifurcation parameter of system, two different types of non-circular bearings are studied. The detailed data are as follows:

$$\bar{C} = 3 \times 10^{-5} \text{ m}, \qquad \bar{R} = 0.05 \text{ m}, \qquad \lambda = 1,$$

$$\bar{\rho} = 0.001 \text{ mm}, \qquad \bar{\mu} = 1.8 \times 10^{-5} \text{ Kg/m s},$$

$$\bar{P}_a = 1.013 \times 10^5 \text{ N/m}^2.$$

(a)

(b)

For validation of results in dynamical state, fi-
nite difference method has been applied to solve
Reynolds equation and instead of using the Runge–
Kutta method, direct method mentioned in Refs.
[10–15] has been considered to obtain acceleration,
velocity, and displacement of the rotor center. Ta-
ble 1 compares the results obtained for the orbits of
the rotor center by two methods under conditions that
a static load and mass of the rotor are chosen to be
$\bar{W}_0 = 506.5$ N and $\bar{m}_r = 25.82$ Kg. Also, the bearing
number is taken to be $\Lambda = 25$. It is observed that a
good agreement exists between two methods.

4.1 Type 1

Three-lobe noncircular gas bearing is loaded by a sta-
tic load of $\bar{W}_0 = 506.5$ N, mass of the rotor is chosen
to be $\bar{m}_r = 25.82$ Kg, and the bearing number is taken
to be $\Lambda = 25$.

4.1.1 Dynamic orbit

Figures 2.1(a) through 2.8(a) show the rotor center or-
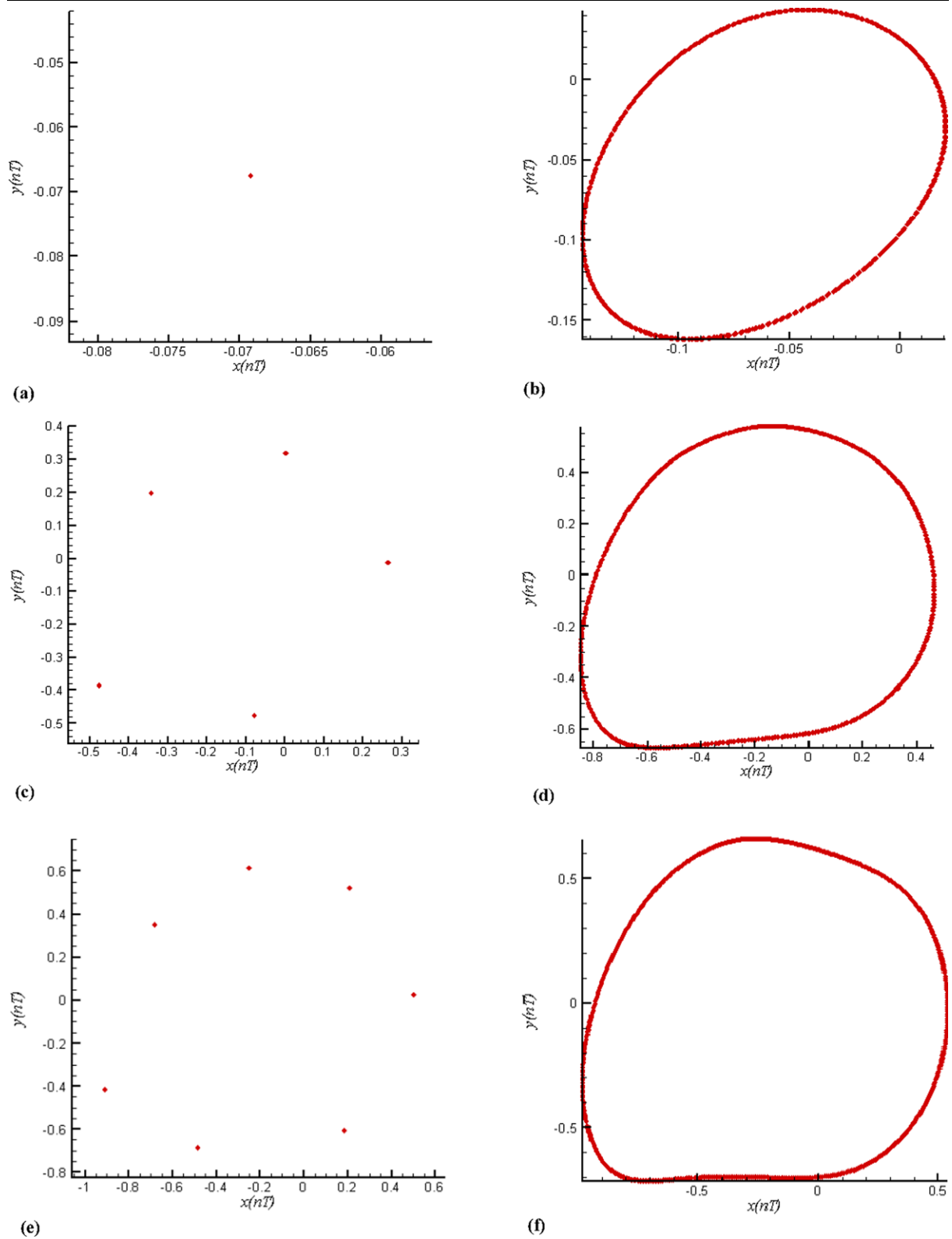bits for different values of the preload. Regular mo-

Fig. 5 Poincare maps of the rotor center trajectory at (**a**) $\delta = 0.52$, (**b**) 0.54, (**c**) 0.544, (**d**) 0.55, (**e**) 0.554, (**f**) 0.56, (**g**) 0.576, (**h**) 0.584
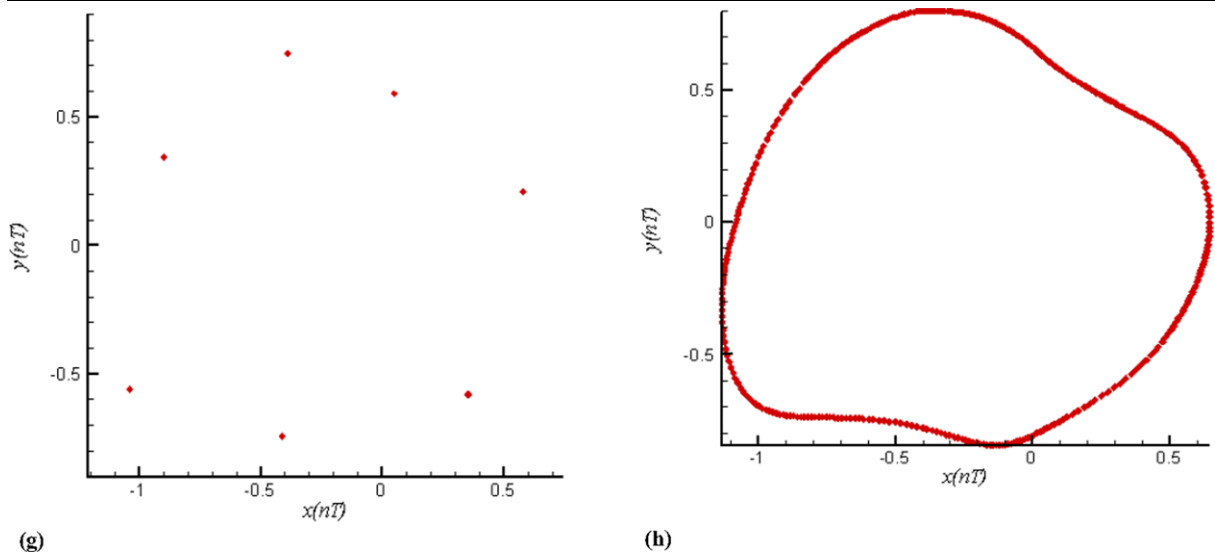
(g)

(h)

Fig. 5 (*Continued*)

tion is shown at $\delta = 0.48$. But, regular motion loses its stability and becomes irregular when the preload is increased to $\delta = 0.542$. The rotor center orbit becomes two closed circles at $\delta = 0.544$ and by increasing preload value to $\delta = 0.55$ irregular motion can be observed again. The rotor center orbit loses irregularity at $\delta = 0.554$ while at $\delta = 0.56$ irregular motion appears again. Regularity in the rotor center orbit increases at $\delta = 0.576$, but irregular motion can be seen at $\delta = 0.584$.

From Figs. 2.1(b) through 2.8(b), it is observed that the phase portrait of the rotor center is regular at $\delta = 0.48$ then becomes irregular at $\delta = 0.542$. It can also be seen that the phase portrait of the rotor center becomes two closed circles at $\delta = 0.544$ and by increasing preload value to $\delta = 0.55$ irregular motion appears again. But the phase portrait of the rotor center loses irregularity at $\delta = 0.554$ while irregular motion can be seen at $\delta = 0.56$ again. Regularity in the phase portrait increases at $\delta = 0.576$, but irregular motion appears at $\delta = 0.584$.
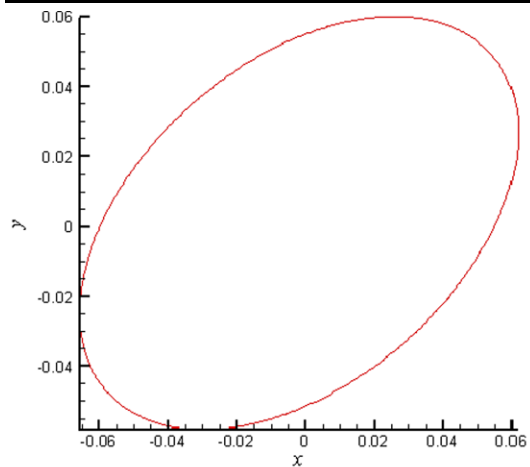
4.1.2 Power spectrum

Figures 2.1(c, d) through 2.8(c, d) show the dynamic responses of the rotor center in horizontal and vertical directions. It is found that the frequency responses of the rotor center demonstrate harmonic motion for the preload value of $\delta = 0.48$ in the both directions.

The frequency responses of the rotor center become quasi-periodic motion at $\delta = 0.542$. But they become KT-periodic motion at $\delta = 0.544$. By increasing the preload value to $\delta = 0.55$, the frequency responses of the rotor center become quasi-periodic motion and this behavior can be substituted by KT-periodic motion at $\delta = 0.554$. At $\delta = 0.56$, the frequency responses of the rotor center become quasi-periodic motion again. By increasing the preload value to $\delta = 0.576$, the frequency responses of the rotor center become KT-periodic motion and this behavior can be substituted by quasi-periodic motion at $\delta = 0.584$.

4.1.3 Bifurcation diagram and Poincare map

The bifurcation diagram is a useful means to observe nonlinear dynamic behavior. By considering preload value as a parameter of system, qualitatively different behavior can be observed in Fig. 3 at the range $0.4 \leq \delta \leq 0.588$. Local bifurcation of the rotor center in the preload range $0.532 \leq \delta \leq 0.588$ is shown in Fig. 4. Results show that, before $\delta = 0.54$, the system has periodic motion in horizontal and vertical directions. Figure 5(a) shows the Poincare maps at $\delta = 0.52$. One point in this map confirms T-periodic motion of the rotor in the both directions. It can be observed that quasi-periodic motion occurs in the interval $0.54 \leq \delta \prec 0.544$. The Poincare map at $\delta = 0.54$ is shown in Fig. 5(b) and closed curve formed in this map
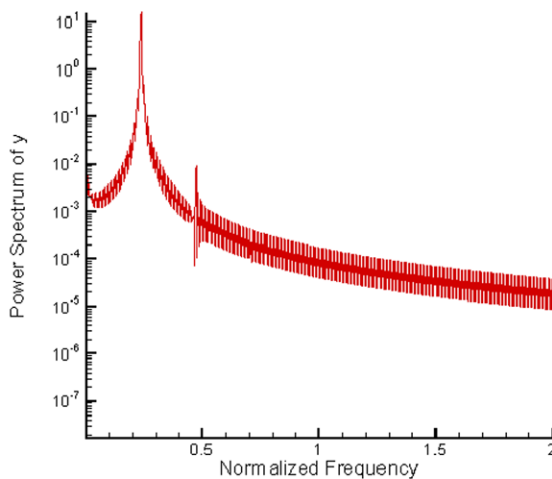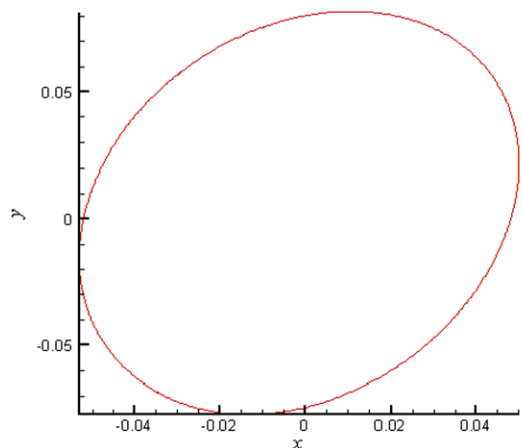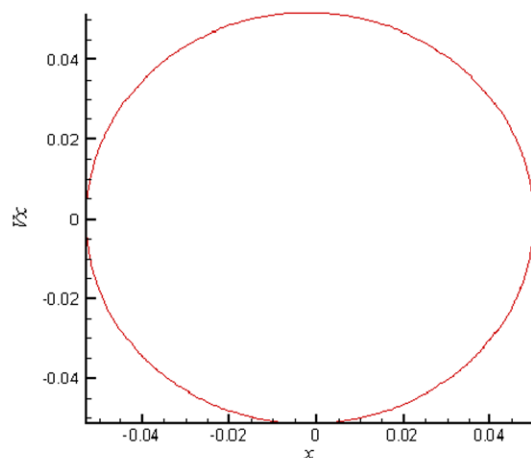
6.1(a)
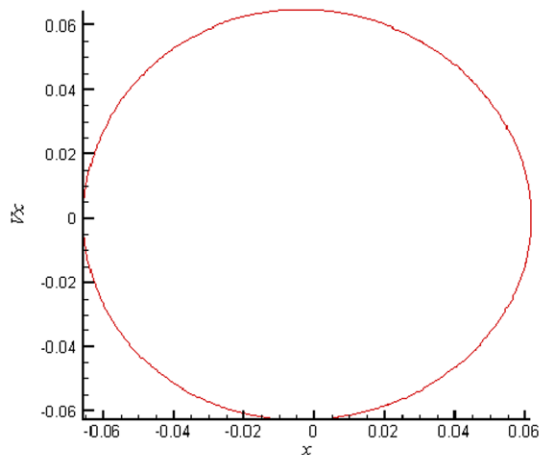
6.1(b)
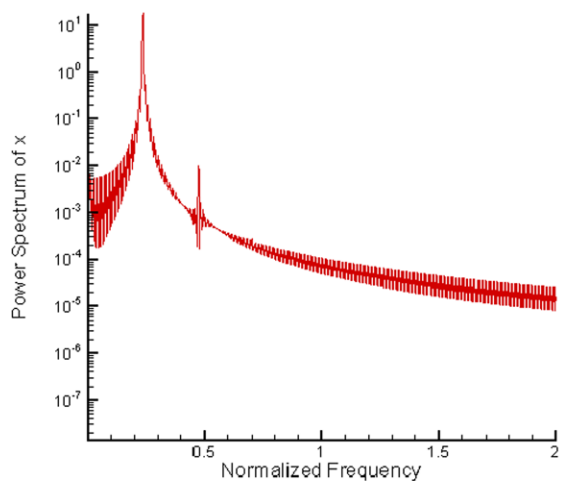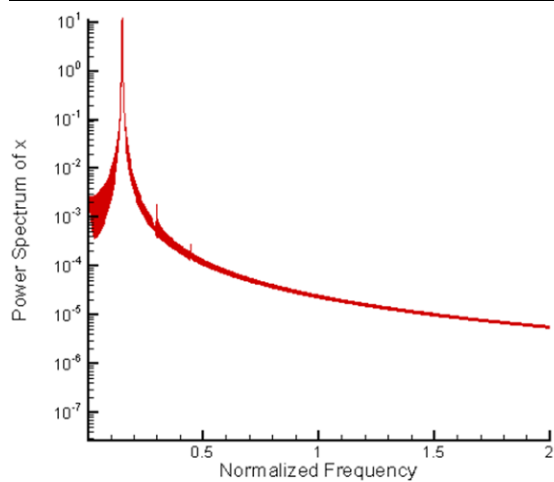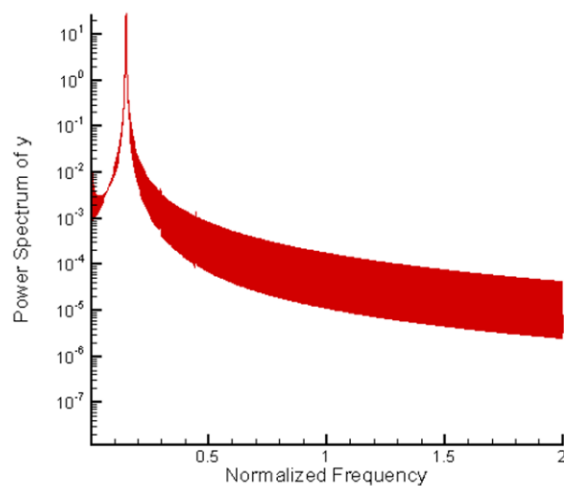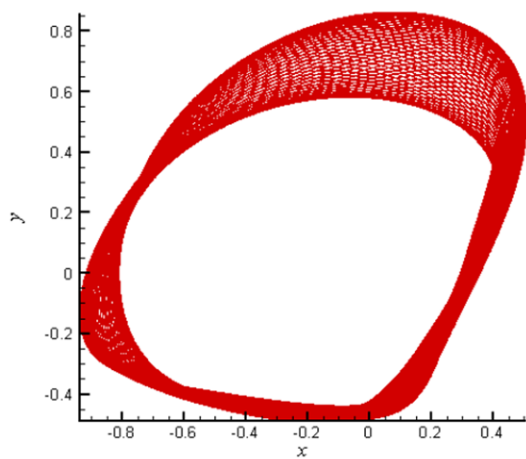

6.1(c)

6.1(d)

6.2(a)

6.2(b)

Fig. 6 Trajectory of the rotor center at $\delta = 0.46, 0.58, 0.608$ and 0.62 (**6.1(a)**–**6.4(a)**); phase portraits of rotor center (**6.1(b)**–**6.4(b)**) and power spectra of rotor displacement in horizontal (**6.1(c)**–**6.4(c)**) and vertical (**6.1(d)**–**6.4(d)**) directions for four-lobe bearing
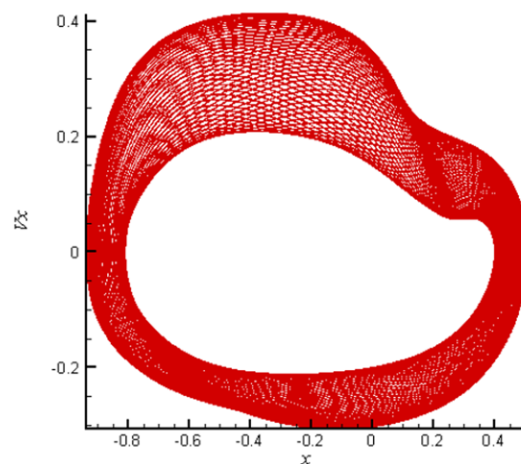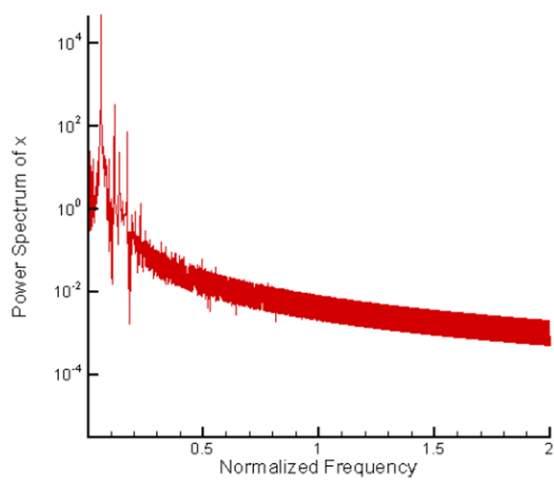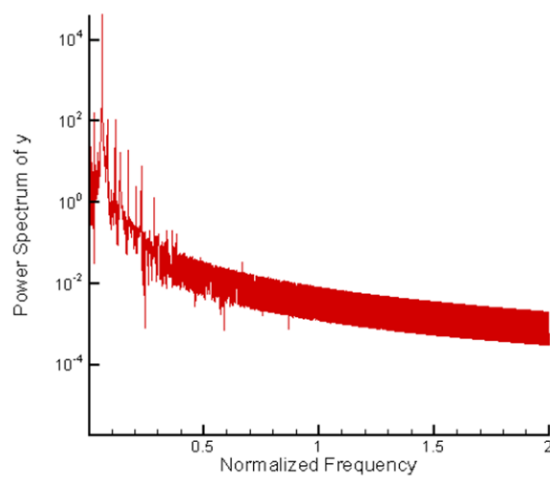
6.2(c)

6.2(d)

6.3(a)

6.3(b)

6.3(c)

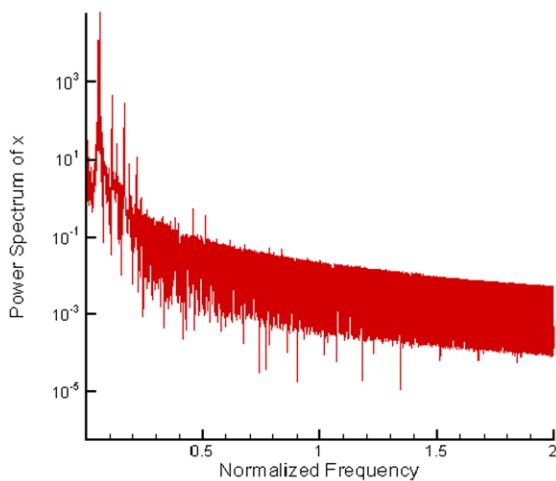**6.3(d)**
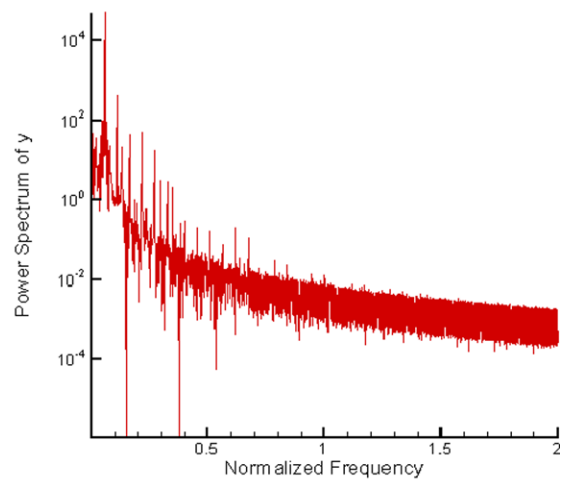
Fig. 6 (*Continued*)
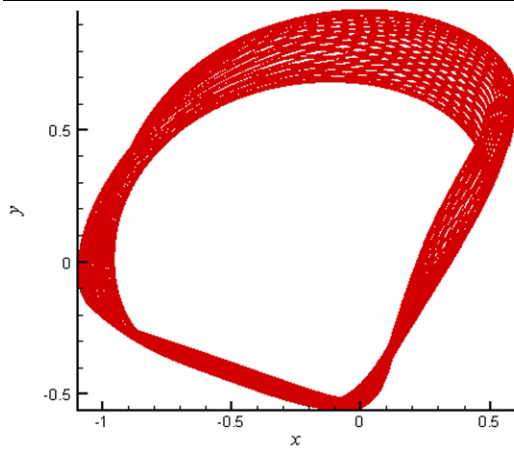
6.4(a)
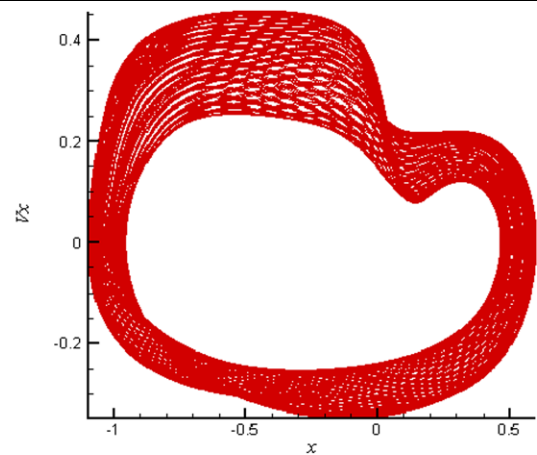
6.4(b)

6.4(c)

6.4(d)

Fig. 6 (*Continued*)

demonstrates quasi-periodic motion of the rotor center at this value of preload. $5T$-periodic motion occurs in the interval $0.544 \leq \delta \prec 0.546$ and five discrete points in Fig. 5(c) confirms this behavior at $\delta = 0.544$. The system is irregular in the range $0.546 \leq \delta \leq 0.552$ and closed curved is shown in Fig. 5(d) demonstrate quasi-periodic motion at $\delta = 0.55$. In the range $0.552 \prec \delta \prec 0.556$, $7T$-periodic motion occurs and Fig. 5(e) confirms this behavior at $\delta = 0.554$. Quasi-periodic motion can be seen in the range $0.556 \leq \delta \leq 0.574$ and Fig. 5(f) demonstrates this motion at $\delta = 0.56$. $7T$-periodic motion occurs in the interval $0.574 \prec \delta \prec 0.58$ and seven discrete points in Fig. 5(g) confirms this behavior at $\delta = 0.576$. But in the range $0.58 \leq \delta \leq$ 0.588, quasi-periodic motion can be seen and Fig. 5(h) demonstrates this motion at $\delta = 0.584$.

4.2 Type 2

In the second case, four-lobe noncircular gas bearing is loaded by a static load of $\bar{W}_0 = 506.5$ N, the mass of the rotor is chosen to be $\bar{m}_r = 25.82$ Kg and the bearing number is taken to be $\Lambda = 25$.

4.2.1 Dynamic orbit

Figures 6.1(a) through 6.4(a) show the rotor center orbits at different values of the preload. Regular motion is shown at $\delta = 0.46$ and 0.58. But regular motion loses its stability and becomes irregular when

Fig. 7 Bifurcation
diagrams: (**a**) $x(nT)$ and
(**b**) $y(nT)$ versus preload
for four-lobe bearing

(a)

(b)
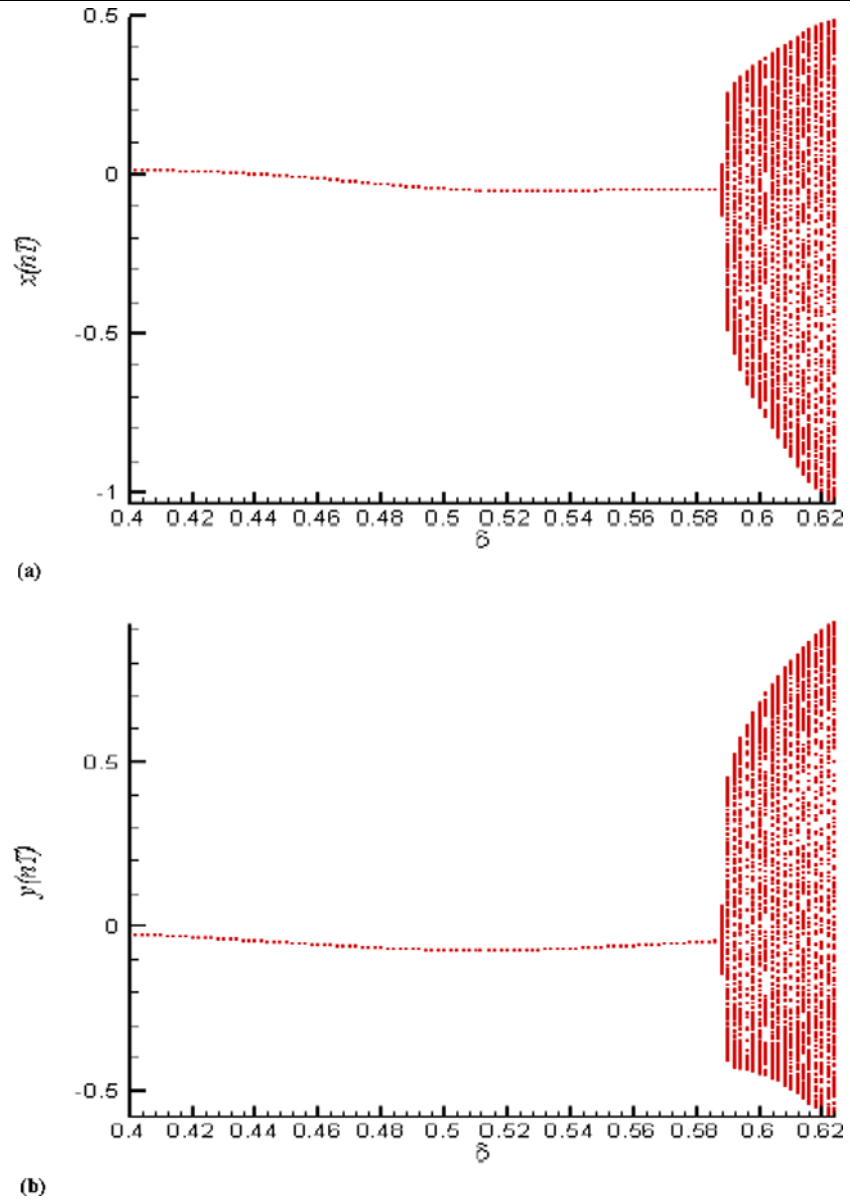
the preload is increased to $\delta = 0.608$ and 0.62. This
condition persists for all preload values in the range
$0.588 \leq \delta \leq 0.628$.

From Figs. 6.1(b) through 6.4(b), it is observed that
the phase portraits of the rotor center are regular at
$\delta = 0.46$ and 0.58 then become irregular at $\delta = 0.608$
and 0.62.

4.2.2 Power spectrum

Figures 6.1(c, d) through 6.4(c, d) show the dynamic
responses of the rotor center in horizontal and verti-

cal directions. It is found that the frequency responses
of the rotor center demonstrate harmonic motion for
the preload values $\delta = 0.46$ and 0.58 in the both di-
rections. But they become quasi-periodic motion at
$\delta = 0.608$ and 0.62.

4.2.3 Bifurcation diagram and Poincare map

By considering preload value as a parameter of sys-
tem, qualitatively different behavior can be observed
in Fig. 7 at the range $0.4 \leq \delta \leq 0.628$. Local bifur-
cation of the rotor center in the preload range $0.58 \leq$

Fig. 8 Local bifurcation diagrams of (**a**) $x(nT)$ and (**b**) $y(nT)$ versus preload for four-lobe bearing

(a)

(b)
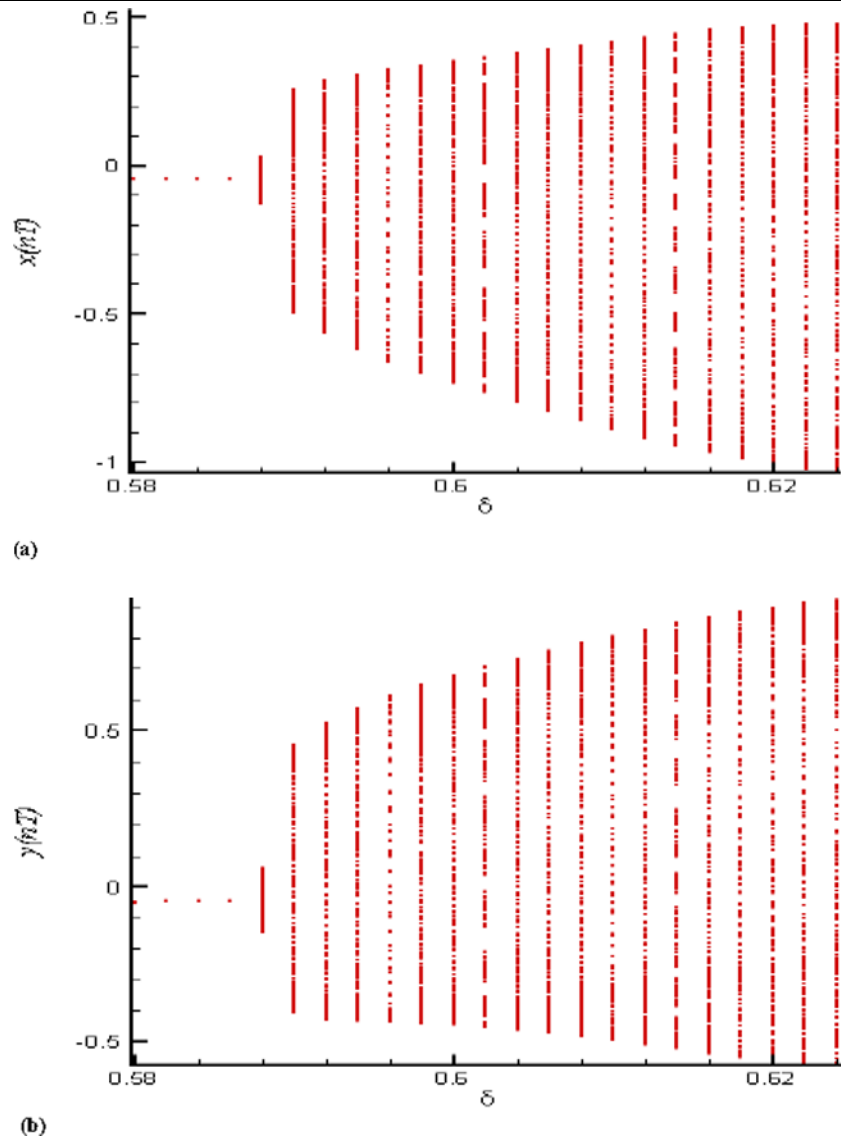
$\delta \leq 0.628$ is shown in Fig. 8. Results show that before $\delta = 0.588$, the system has periodic motion in the horizontal and vertical directions. Figures 9(a) and (b) show the Poincare maps at $\delta = 0.46$ and 0.58, respectively. One point in these maps confirms T-periodic motion of the rotor in the both directions. It can be seen that quasi-periodic motion occurs in the interval $0.588 \leq \delta \leq 0.628$. The Poincare maps at $\delta = 0.608$ and 0.62 are shown in Figs. 5(c) and (d), respectively. Closed curve formed in these maps demonstrate quasi-periodic motion of the rotor center at these values of preload.

5 Conclusions

In this study, the effect of preload on nonlinear dynamic behavior of a rigid rotor supported by noncircular gas-lubricated journal bearings has been studied. Two types of noncircular bearing such as three and four-lobe bearings have been considered. Due to nonlinearity of the gas film force, computational methods have been employed to study the dynamical behavior of the system. Dynamical orbits, power spectra, Poincare maps, and bifurcation diagrams are used to identify the dynamic behavior of these systems.
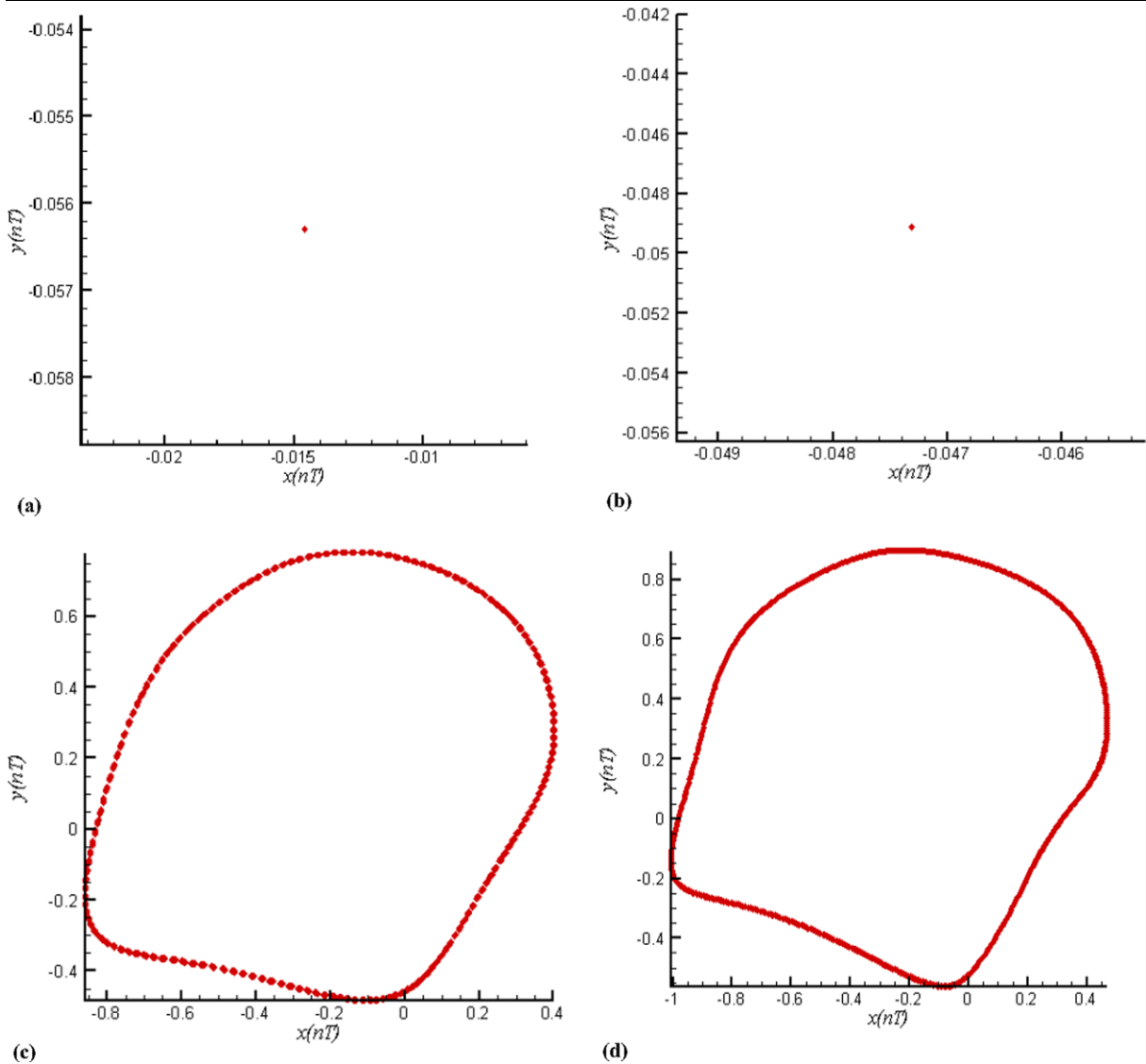
Fig. 9 Poincare maps of the rotor center trajectory at (**a**) $\delta = 0.46$, (**b**) 0.58, (**c**) 0.608, (**d**) 0.62

From this study, it is shown that by considering the preload value as a parameter of the system, periodic, KT-periodic, and quasi-periodic motions occur in both three and four-lobe bearings. By comparing two types of bearings, it can be seen that at preload values that irregular motion occurs in three-lobe bearing; four-lobe bearing has regular motion.

The variation of this parameter plays a major role in noncircular bearing systems and its influence varies with the number of lobes of the noncircular journal bearings. Thus, by selecting proper type of bearing and changing the system parameter to suitable values, rotor center can be avoided from the undesirable behavior.

References

1. Castelli, V., Elrod, H.G.: Solution of the stability problem for 360 degree self-acting, gas-lubricated bearing. ASME J. Basic Eng. **87**, 199–212 (1961)
2. Ausman, J.S.: Linearized PH stability theory for translatory half-speed whirl of long self-acting gas-lubricated journal bearings. ASME J. Basic Eng. **83**, 611–619 (1963)

3. Holmes, A.G., Ettles, C.M., Mayes, I.W.: Aperiodic behavior of a rigid shaft in short journal bearings. Int. J. Numer. Methods Eng. **12**, 695–702 (1978)

4. Chandra, M., Malik, M., Sinhasan, R.: Comparative study of four gas-lubricated noncircular journal bearing configuration. Tribol. Int. **16**, 103–108 (1983)

5. Zhao, J.Y., Linnentt, I.W., Melean, L.J.: Subharmonic and quasi-periodic motion of an eccentric squeeze film damper-mounted rigid rotor. ASME J. Vib. Acoust. **116**, 357–363 (1994)

6. Adiletta, G., Guido, A.R., Rossi, C.: Chaotic motion of a rigid rotor in short journal bearings. Nonlinear Dyn. **10**, 251–269 (1996)

7. Adiletta, G., Guido, A.R., Rossi, C.: Nonlinear dynamics of rigid unbalanced rotor in short bearings. Part I: Theoretical analysis. Nonlinear Dyn. **14**, 57–87 (1997)

8. Adiletta, G., Guido, A.R., Rossi, C.: Nonlinear dynamics of rigid unbalanced rotor in short bearings. Part II: Experimental analysis. Nonlinear Dyn. **14**, 157–189 (1997)

9. Czolczynski, K., Kapitaniak, T.: Hopf bifurcation in rotors supported in gas bearings. Chaos Solitons Fractals **4**, 499–515 (1997)

10. Wang, C.C., Chen, C.K.: Bifurcation analysis of self-acting gas journal bearings. J. Tribol. **123**, 755–767 (2001)

11. Wang, C.C., Jang, M.J., Chen, C.K.: Nonlinear dynamic analysis of a flexible rotor supported by self-acting gas journal bearing. Proc. Inst. Mech. Eng. **12**, 1527–1538 (2004)

12. Wang, J.S., Wang, C.C.: Nonlinear dynamic and bifurcation analysis of short aerodynamic journal bearings. Tribol. Int. **38**, 740–748 (2005)

13. Wang, C.C.: Nonlinear dynamic behavior and bifurcation analysis of a rigid rotor supported by relatively short externally pressurized porous gas journal bearing system. Acta Mech. **183**, 41–60 (2006)

14. Wang, C.C.: Bifurcation analysis of an aerodynamic journal bearing system considering the effect of stationary herringbone grooves. Chaos Solitons Fractals **33**, 1532–1545 (2007)

15. Wang, C.C., Yau, H.T., Jang, M.J., Yeh, Y.L.: Theoretical analysis of the non-linear behavior of a flexible rotor supported by herringbone grooved gas journal bearings. Tribol. Int. **40**, 533–541 (2007)

16. Rahmatabadi, A.D., Rashidi, R.: Effect of mount angle on static and dynamic characteristics of gas-lubricated, noncircular journal bearings. Iran. J. Sci. Technol. **37**, 27–37 (2006)

17. Rahmatabadi, A.D., Rashidi, R.: Investigation of preload effects on noncircular gas bearing systems performance. J. Appl. Sci. Technol. **4**, 33–38 (2007)